Integrating Visible, Near-Infrared, and Short-Wave Infrared Hyperspectral and Multispectral Thermal Imagery for Geologic Mapping: Simulated Data

Xianfeng Chen, Timothy A. Warner, and David J. Campagna

Department of Geology and Geography
West Virginia University
Morgantown, West Virginia 26506-6300

1. Introduction

Recent developments in VNIR/SWIR[1] hyperspectral and TIR multispectral remote sensing have greatly increased the potential for accurate geological mapping. Hyperspectral instruments, often referred as imaging spectrometers, acquire image data simultaneously in many narrow, contiguous channels (Goetz et al., 1985), generally spanning the reflected solar portion of the electromagnetic spectrum (0.4–2.5 µm) (Vane et al., 1993). The spectral bandwidths of hyperspectral image bands are generally less than 25 nm, in order to facilitate the identification of diagnostic absorption features of minerals (Clark, 1999). Hyperspectral data have a significant advantage over conventional multispectral data, such as Landsat Thematic Mapper imagery, in that with hyperspectral data, minerals can be identified by comparisons with generic library spectra (Clark et al., 2003). With hyperspectral data, it is therefore theoretically possible to map the surface mineralogy of an area without acquiring any ground data from the particular site.

In contrast to the many bands of hyperspectral instruments, TIR multispectral sensors measure surface radiance in a small number of broad bands. TIR imagery provides important information regarding temperature, thermal inertia, and emissivity of ground materials (Price, 1979; Kahle, 1987; Warner and Chen, 2001). Surface emissivity is potentially the most useful thermal property because it is an inherent characteristic of an object and is independent of illumination intensity and local temperature. Emissivity is defined as the ratio of the emitted radiation to that of a blackbody at the same temperature (Hook et al., 1992). Emissivity can be used to identify individual minerals and has been related to silica content of rocks (Lyon, 1972), thus offering the possibility of discriminating the silicate materials that make up much of the land surface.

Minerals tend to have characteristic spectral reflectance and associated emissivity features, which may potentially be used for remote identification (Clark, 1999; Hook et al., 1994). The characteristic spectral features are produced by the interaction of electromagnetic energy with the atoms and molecules of the minerals, which cause electronic transitions and vibrational processes. Electronic transitions tend to dominate mineral spectra in the visible and NIR, but are also found across the SWIR region (Clark, 1999; Goetz, 1989). Vibrational processes, dominating in SWIR and TIR region, produce particularly diagnostic absorption features in the spectra of silicate, hydroxyl, oxide, carbonate and water-bearing minerals (Vincent and Thomson, 1971; Hunt and Salisbury, 1974; Hunt, 1980; Hook et al., 1994; Clark, 1999).

---

[1] An unfortunate inconsistency has developed in the terms used by the remote sensing community for regions of the electromagnetic spectrum (Clark, 1999). In this study, the wavelength regions are defined as follows: **visible**: 0.4–0.7 µm, **near-infrared (NIR)**: 0.7–1.1 µm, **visible and near-infrared (VNIR)**: 0.4–1.1 µm, **short-wavelength infrared (SWIR)**: 1.1–2.5 µm, **mid-infrared (MIR)**: 3–5 µm, and **thermal infrared (TIR)**: 8–14 µm (Goetz, 1989; Hook *et al*., 2001).

The distinctive spectral features of silicates, as well as other important spectral features of most non-silicate minerals, including the carbonates, sulfates, phosphates, oxides, and hydroxide mineral groups, demonstrate the tremendous potential of the TIR region for geological mapping. Combining information from TIR spectral emissivity with measurement of spectral reflectance in the 0.4–2.5 μm region, which is particularly good for discriminating clays, iron oxides, and iron hydroxides (Clark, 1999), should provide a more comprehensive overview of rock compositional information than using data from only one of the two regions (Rowan, 1998).

In summary, the combination of VNIR/SWIR hyperspectral data and TIR multispectral data appears to have great promise for geological studies because of the complementary nature of information from the thermal and shorter wavelengths (Hook et al., 1999). Typically, iron oxide, hydroxyl, and carbonate minerals have absorption features in the visible or SWIR region, while the Si-O bonding of silicate minerals exhibit absorption features in TIR region. Nevertheless, combining VNIR/SWIR and TIR data has received very little prior attention, with the exception of Abrams and Hook (1991), who separately analyzed VNIR/SWIR hyperspectral and TIR multispectral data for lithological analysis at Cuprite, Nevada.

That no previous research has simultaneously analyzed VNIR/SWIR hyperspectral and TIR multispectral data is probably due to the fact that data from these spectral regions are rarely acquired simultaneously, and that coregistration of aerial imagery from different sources can be very challenging. However, modern aircraft-acquired data often include navigation information that can be used to remove non-systematic spatial distortions. Furthermore, in the future, with the increased availability of satellite data, which tends to have simpler geometry than aerial imagery, coregistration of different image products may become more routine. In fact, space-borne hyperspectral data is already being collected by the Hyperion instrument, and space-borne multispectral TIR data by the Advanced Spaceborne Thermal Emission and Reflection Radiometer (ASTER). Integrating imagery from different sensors may not even be necessary in the future; for example there are plans to fly an airborne hyperspectral sensor in 2005, Airborne Reflective Emissive Spectrometer (ARES), which has 160 image bands in the visible, NIR, SWIR, and TIR wavelength regions (Mueller *et al*., 2003).

This study investigated the potential value of integration of VNIR/SWIR hyperspectral analysis with TIR multispectral analysis, with the anticipation that such an approach should provide improved geological mapping. To test this hypothesis, simulated data were used to test the improvement in classification accuracy when the combination of VNIR/SWIR hyperspectral and TIR multispectral data is used, compared to an analysis that uses only the VNIR/SWIR or TIR regions on their own. In addition, the simulated data were used to evaluate the performance of automatic information extraction algorithms, including the conventional classification algorithms of minimum distance and maximum likelihood classification (Richards, 1993), as well as the hyperspectral analysis techniques of spectral angle mapper (Kruse et al., 1993a), binary encoding (Goetz et al., 1985), and spectral feature fitting (Crowley et al., 1989; Clark et al., 1990).

Simulated data have been demonstrated to be useful in developing general theories about how information is represented in images and spectra (Strahler et al., 1986). For example, simulated data have been used in many studies of image spatial properties (e.g., Woodcock et al., 1988, Jupp et al., 1989, Collins and Woodcock, 1999, Warner, 1999, Ferro and Warner, 2002), and spectral properties (e.g., Verhoef, 1984, Li et al., 1999, Pandya et al., 2000).

Simulated data were chosen for this study because with simulated data it is possible to evaluate accuracy with complete confidence in the reference data set. In contrast, ground checking of minerals for real hyperspectral analyses is challenging, especially when the minerals are fine grained. Although minerals can be identified through laboratory techniques, it is hard to generalize from small laboratory samples to 20 meter pixels, and especially difficult to estimate the proportions of minerals present in fine mixtures. Additional uncertainty is added by varying desert varnish, vegetation, weathering, and deposition of transported material in each pixel. Thus, in summary, it is close to impossible to produce a "truth map" for geological hyperspectral remote sensing; and indeed, we know of no previous quantitative assessment of accuracy of geological hyperspectral remote sensing classification.

A second reason for using simulated data is that this approach allows us to vary image properties in a controlled fashion, and thus potentially develop an understanding of the reasons behind the results we observe. We are also able to study what aspects of the scene model most affect the different methods, a key to developing improvements to the different methods. For example, if illumination variation were found to be a major source of error, then we would infer that illumination normalization methods should be researched further.

The third reason for using simulated data is that simulation provides a simplified, but reasonable, representation of real data as long as the major processes that result in a real image are included in the analysis. Simulated data are typically much simpler than reality. This does not necessarily negate the value of simulated data; indeed, the simplification can be an advantage, as discussed above.

In a future paper, the classification methods tested in this paper, as well as a specially developed expert system, will be applied to real data, comprising AVIRIS (Airborne Visible/Infrared Imaging Spectrometer) and MASTER (MODIS/ASTER Airborne Simulator) imagery of Cuprite, Nevada.

2. Methods

2.1 Classification algorithms

Image classification methods can be divided into two groups: **empirical classification algorithms** that use summary class statistics based on groups of image pixels, and **spectral analysis techniques** that match image spectra to previously acquired field or laboratory spectra, known as spectral libraries. With hyperspectral data, empirical classification approaches that rely on statistical measures tend to require excessive numbers of training samples for training the classifier (Landgrebe, 2000). The spectral library approach is attractive for hyperspectral image analysis because rocks and minerals tend to have distinctive and consistent spectral absorption features, as discussed above. Furthermore, the potential to identify surface materials without any local field data is clearly very attractive.

The two most common empirical classification methods used for geological mapping are minimum distance and maximum likelihood classification. Numerous additional spectral analysis methods have been developed for geological mapping (Mustard and Sunshine, 1999), including binary encoding, spectral feature fitting, and the spectral angle mapper. These three spectral analysis methods will be described briefly below.

Binary encoding (Goetz et al., 1985) is a fast spectral matching algorithm that compares summary measures of the spectral shapes of an unknown pixel and the reference spectra. The unknown pixel spectrum of n bands is represented by an n bit vector, with each bit set to 1 or 0 respectively, depending on whether the value of the spectrum for that band is above or equal to, or below the pixel mean.

Spectral feature fitting (SFF) (Crowley et al., 1989; Clark et al., 1990) is based on a comparison of the absorption features in the image and reference spectra. The continuum, defined as a convex hull fit over the top of each spectrum utilizing straight line-segments to connect local spectrum maxima (Clark et al., 2003; Kruse et al., 1993b), is removed by dividing the convex hull into the original spectrum. The continuum-removed pixel spectrum and reference spectra are compared at each absorption band using a least-square fit. The root mean square error indicates the relative goodness-of-fit of the two spectra.

Spectral angle mapper (SAM) (Kruse et al., 1993a) builds on the hyperspherical direction cosine method (Pouch and Campagna, 1990) by calculating the similarity between pixel spectra and reference spectra in terms of the angle between two n-dimensional vectors, where n is the number of bands of hyperspectral data.

2.2 Simulated data

The creation of the simulated data was carried out using the Interactive Data Language (IDL) (Research Systems, 2000). The spectra of 16 common minerals, rock types, and alteration types (Table 1) were chosen for this study because they represent the dominant lithological units and alteration types typical of hydrothermal alteration areas such as Cuprite, Nevada (Abrams and Ashley, 1980). The library spectra were resampled to match the approximate spectral bandwidth and signal-to-noise of the AVIRIS and MASTER instruments. A brief introduction to the AVIRIS and MASTER instruments is given below (see also Table 2), followed by a more detailed discussion of the simulated data characteristics.

Table 1. Minerals, rock types, and alteration types used to create the simulated data

Type	**Name**
Minerals	Quartz, calcite, hematite, goethite, alunite, kaolinite, montmorillonite, muscovite, gypsum.
Unaltered rocks	Basalt, limestone, sandstone, siltstone
Altered rocks	Silicified rocks, opalized rocks, and argillized rocks.

The MASTER sensor was developed to support research prior to the launch of the Advanced Spaceborne Thermal Emission and Reflection Radiometer (ASTER) and the Moderate Resolution Imaging Spectroradiometer (MODIS) (Hook et al., 2001). MASTER has a total of 50 bands from 0.4–13 µm, including 10 TIR bands. In this study, simulated multispectral thermal data are based only on the 10 MASTER TIR bands (7.6–13 µm). AVIRIS, flown by NASA since 1987 (Green et al., 1998), acquires data in 224 narrow, contiguous spectral bands across the reflected solar energy region (0.4–2.5 µm), each band approximately 10 nm at full width, half maximum (FWHM).

Table 2. Summary characteristics of the MASTER and AVIRIS instruments

Characteristic	**Sensor**	
	MASTER	**AVIRIS**
Wavelength range	0.4–13 µm	0.4–2.5 µm
Number of spectral bands	50	224
Channel width	Varies, 40 to 650 nm	10 nm
Instantaneous field of view	2.5 mrad	1 mrad
Total field of view	85.92º	33º
Number of pixels	716	614
Platform	B200, ER-2, DC-8	ER-2, Twin Otter
Digitization	16-bit	12-bit

The simulated data were derived from the public domain spectral library included with ENVI (Research Systems, 2002): the Johns Hopkins University library of spectra of materials from 0.4 to 14 µm (Salisbury et al., 1991; Research Systems, 2002). Emissivities of minerals or rocks are calculated from Kirchoff's law, which states that spectral emissivity equals 1 minus the spectral reflectance.

To simplify the simulated data construction, the contribution of the atmosphere was not modeled directly. Nevertheless, the effects of the atmosphere were included indirectly, because noise was added on a band-by-band basis, equivalent to that found in typical AVIRIS and MASTER scenes that include atmospheric effects. In addition, the simulated AVIRIS bands in the atmospheric water absorption regions near 1.4, 1.9, and 2.5 µm were deleted, leaving a total of 188 out of the 224 bands for the analysis. Multiplying the spectral radiances with the inverse of the spectral signal-to-noise ratios for

AVIRIS and MASTER simulated the noise of the sensor system. The signal-to-noise ratio of AVIRIS was taken from Green et al. (1998), who measured in the laboratory the average and standard deviation of 3000 dark signal spectra, and 3000 illuminated radiometric calibration target spectra. The signal-to-noise ratio of MASTER was estimated using the ratio of the mean and standard deviation of a 7 by 7 moving window of MASTER imagery of Lake Mead, Nevada. An additional 0.015 variation in emissivity (Gillespie et al., 1998) was added to simulate the uncertainty due to the indeterminacy of the emissivity calculation from radiance data.

The library spectra were also combined in various proportions to simulate real pixels, which generally comprise mixed proportions of different surface materials:

$$L_{\lambda} = \sum_{i=1}^{n} \left(a_i R_{\lambda \mathrm{i}} \right) + \varepsilon_{\lambda} \tag{1}$$

Where

L_{λ} = reflectance or emissivity at wavelength λ corresponding to a specific AVIRIS or MASTER band;

a_i = the proportion of the endmember i in the pixel;

$R_{\lambda i}$ = the reflectance or emissivity of endmember i at wavelength λ;

ε_{λ} = the error term resulting from all sources of noise at wavelength λ.

Seven groups of simulated data with different levels of uncertainties were derived using equation 1 (Table 3). Each group includes three data sets designed to simulate AVIRIS data (188 bands between 0.4–2.5 µm, after the exclusion of the water absorption bands), MASTER thermal data (10 bands between 7.6–13 µm), and the combination of AVIRIS and MASTER multispectral thermal infrared data (a total of 198 bands between 0.4–2.5 µm and 7.6–13 µm). The simulated uncertainties include sensor system noise, mixing of vegetation and the other endmembers, and variation in solar illumination. Solar illumination uncertainty was applied only to the simulated AVIRIS data, assuming that topographic effects in thermal data are mostly suppressed when the emissivity is calculated. Solar illumination effects were simulated by varying the total radiance by 0 to 25 percent. The first group of data is a theoretical

Table 3. Simulated data with different levels of uncertainties*

Group	**Simulated Noise**			
	System	**Solar Illumination**	**Mixed pixels (proportion of cover type)**	
			Vegetation	**Additional mineral/rock**
1	X			
2	X	X		
3	X		0–5%	
4	X		0–5%	0–10%
5	X	X	0–5%	0–10%
6	X	X	0–5%	0–20%
7	X	X	0–10%	0–30%

*Empty boxes indicate uncertainties not included in the simulated data.

near-perfect data set, containing only reflectance or emissivity information and system noise of sensor instruments. The uncertainties of the second group include the system noise and solar illumination effects; in the third group, a random percentage of vegetation, up to 5 percent, is added; the fourth group has a random proportion, up to 5 percent, vegetation, and up to10 percent of another mineral or rock endmember, randomly selected from the 16 library spectra; the fifth group is similar to the fourth, except it also includes variations in solar illumination; the sixth group has up to 5 percent vegetation and up to 20 percent of another mineral or rock endmember, and the illumination effects; the seventh group has up to 10 percent vegetation, up to 30 percent another endmember, and illumination effects.

2.3 Analysis

All classification and spectral analysis methods were carried out with ENVI image analysis software (Research System, 2002). Binary encoding, SAM, and SFF were applied using endmember spectra derived from training data and also by comparing the image data directly with the spectral libraries. SFF is normally used with data of more limited spectral regions, and therefore SFF was also tested using the simulated AVIRIS bands from just the SWIR region (1.96–2.44 µm). Considering that SFF's focus on spectral absorption features makes the method inappropriate for use with minerals and rocks with spectrally flat curves, additional comparisons were made using only the nine minerals which exhibit absorption features in VNIR, SWIR, and TIR: alunite, calcite, goethite, hematite, kaolinite, montmorillonite, muscovite, quartz, and gypsum.

Data sets 5, 6 and 7 have comparatively high levels of uncertainty, and were found to produce notably low accuracies, especially for minimum distance and SAM classification. Therefore, additional preprocessing was carried out to evaluate whether the effect of the uncertainty could be reduced for these methods using the minimum noise fraction (MNF) transformation (Green et al., 1988). MNF was used to generate 13 MNF bands for each data set. MNF consists of two cascaded principal component transformations, and is usually used to suppress noise and reduce the number of bands prior to classification. The first transformation decorrelates and rescales the noise in the data, assuming the noise has unit variance and no band-to-band correlation. The second step is a standard principal component transformation applied on the noise-free data. The final transformed data includes two parts: one part associated with large eigenvalues representing most of the variance, and a second part with near-unity eigenvalues representing the noise-dominated data (Green et al., 1988).

Overall accuracies were calculated, and used to evaluate the degree to which the combined data aids discrimination by contributing to increased separability of the entire group of spectral classes. ENVI's confusion matrix procedure (Research Systems, 2002) was applied to all classified images to evaluate the performance of the classifications. The same approximately 10,000 pixels used for training the classifiers were used for classification assessment. In conventional accuracy assessment, different training and testing pixels are normally used. However, in this case, with a large random sample, there would be little difference in the results if a new data set was used for testing.

3. Results

3.1. Evaluation of combining VNIR, SWIR, and TIR spectral regions

The overall accuracies of classifications (Figure 1) were found to vary with the mapping methods and the data sets. With the exception of maximum likelihood, SFF, and all methods using the first uncertainty level data set, most methods applied to simulated MASTER data have higher accuracies than when applied to combined data sets (Figure 1, upper right). Although the simulated MASTER data has few bands, these bands have a higher signal-to-noise ratio than the simulated AVIRIS data due to MASTER's broad bands and the lack of variation in illumination in the simulated TIR data.

Figure 1 nevertheless provides evidence to support the hypothesis that the combination of AVIRIS and MASTER aids discrimination of minerals and rocks. First, for maximum likelihood classification, the combined data set always has the highest overall accuracy of the three data sets. The combined data set also produced the highest accuracy for minimum distance classification and SAM applied to MNF transformed data (Figure 2).

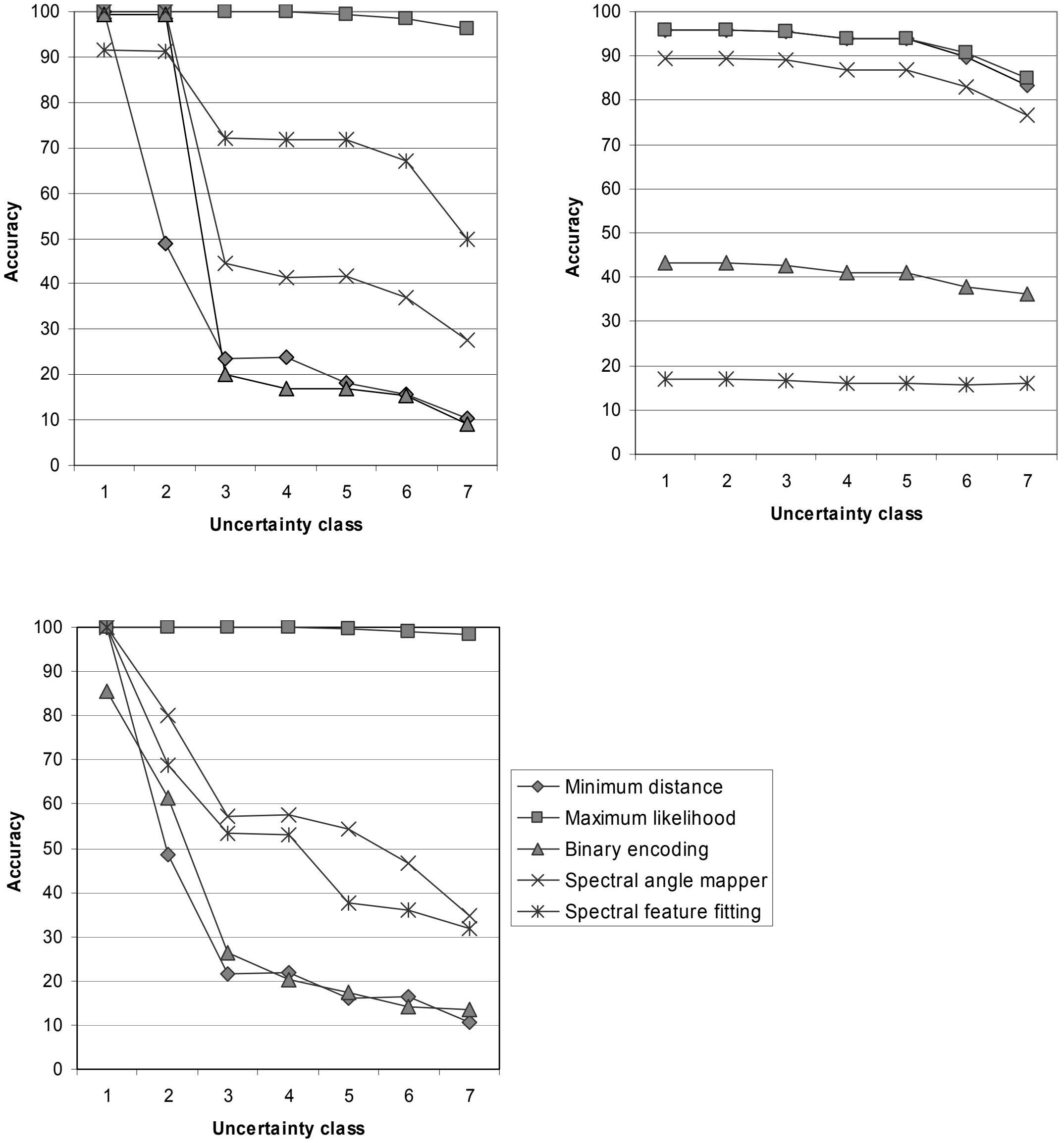

Figure 1. Comparison of the overall accuracies using five mapping methods on different noise level data sets of 16 mineral and rock classes. Upper left: AVIRIS data sets. Upper right: MASTER data set. Bottom: Combined data set.

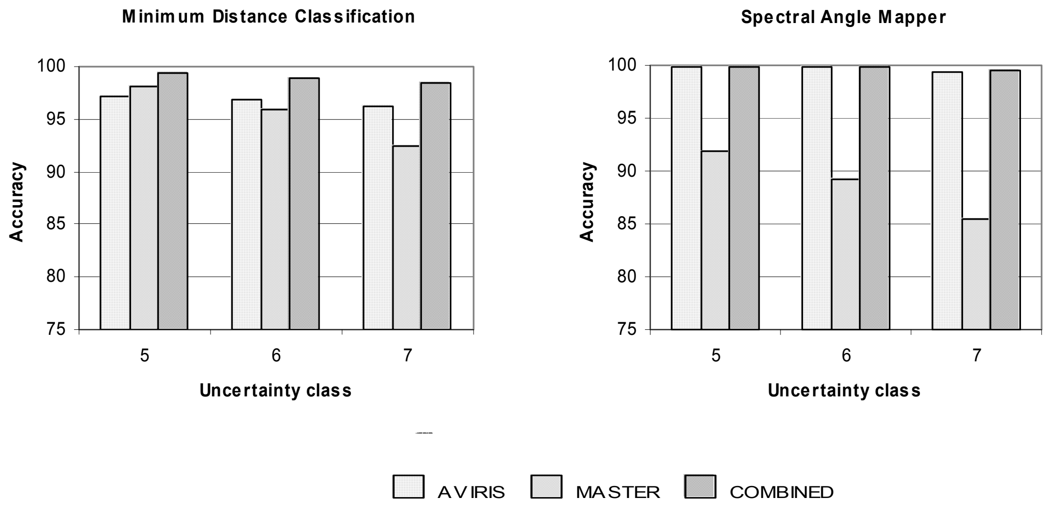

Figure 2. Overall classification accuracies of minimum distance classification and spectral angle mapping applied on MNF transformed data sets (Uncertainty levels 5, 6, and 7).

When the classifications are examined in more detail, some of the individual minerals and rocks can be seen to show large improvement in classification accuracy when the AVIRIS data set was combined with the MASTER data set (Table 4). For instance, basalt, calcite, and muscovite showed an improvement of almost 30 percent in either the producer's accuracy or the user's accuracy when SAM was applied to the combined data set. However, some minerals, such as alunite, montmorillonite, and kaolinite, showed little improvement, or even a decrease in accuracy. Most of the minerals that showed an improvement in classification accuracy with the combined data sets analyzed using SFF classification exhibit the characteristic absorption features in the thermal infrared wavelength region (Figure 3). For example, quartz and muscovite, which have deep Si-O absorption features around 9 μm, showed a marked improvement in classification accuracy using the combined data set. Likewise, goethite and hematite showed a higher classification accuracy with the combined data set because they have absorption features at 12.1 and 8.2 μm, respectively. On the other hand, basalt and kaolinite have relatively flat TIR spectra (Figure 3), so combining AVIRIS and MASTER reduced their classification accuracies. Calcite has only two relative weak absorption features in the 9 and 11 μm wavelength regions, which are diluted by mixing with other minerals or rocks. Therefore, calcite did not show any improvement in classification accuracy within the combined data set. Although alunite and gypsum are characterized by strong absorption features in the TIR, they are too close to be separated in the MASTER data, and therefore the combined data set did not enhance discrimination.

When SFF was applied to the AVIRIS SWIR bands alone (1.96–2.44 μm), the overall accuracy decreased, although some minerals with distinctive absorption features, such as kaolinite (Figure 3), showed a 55 percent improvement in user accuracy. However, some minerals with characteristic absorption features in the VNIR region, for instance, hematite and goethite (Figure 3), showed a large decrease in accuracy (e.g., 65 percent in user accuracy for hematite and 43 percent in producer accuracy for goethite). Thus, as might be expected, SFF applied to a relatively narrow wavelength region only enhances identification of the specific minerals or rocks which exhibit distinctive absorption features in that wavelength region.

Table 4. Classification accuracies of minerals and rock on data set 4 using SAM and SFF

Mineral or rock	**Accuracy: SAM**				**Accuracy: SFF**			
	AVIRIS		**COMBINED**		**AVIRIS**		**COMBINED**	
	Prod.*	**User**	**Prod.**	**User**	**Prod.**	**User**	**Prod.**	**User**
Alunite	30.43	100.00	38.14	92.00	92.38	97.17	44.91	76.67
Basalt	26.72	44.72	66.31	68.00	72.31	74.01	21.85	84.67
Calcite	19.00	52.80	43.19	80.05	79.49	99.94	74.03	96.06
Goethite	53.02	59.30	67.05	67.95	94.81	78.83	85.39	100.00
Hematite	65.90	65.46	69.85	68.98	76.75	95.96	100.00	100.00
Kaolinite	50.64	99.85	65.89	73.96	84.76	44.76	62.09	15.99
Montm.	36.06	53.95	52.69	64.26	81.39	95.58	37.63	99.61
Muscovite	26.19	11.76	61.12	21.93	43.36	62.99	44.43	100.00
Quartz	52.95	16.30	55.40	30.72	68.61	87.00	91.14	100.00
Gypsum	61.55	71.76	70.06	70.11	86.84	99.95	47.65	100.00

*Producer's accuracy of classification.

3.2. Evaluation of classification algorithms

The major uncertainties added to the data sets include variable vegetation coverage, solar illumination effects, and mixing of the other minerals (Table 3). All the classification methods, with the exception of maximum likelihood classification applied to the simulated AVIRIS data sets, are generally very sensitive to the type and degree of uncertainty. For the near-perfect data set of the simulated AVIRIS with only instrumental system noise, all methods achieved relatively high classification accuracies, with maximum likelihood classification, binary encoding, and SAM obtaining 100 percent accuracy (Figure 1). When up to 5 percent mixing of vegetation is added to the data (Uncertainty Level 3), only maximum likelihood classification still resulted in 100 percent accuracy; the accuracies using the other methods dropped rapidly. This suggests that minimum distance classification, binary encoding, and SAM, are very sensitive to subpixel mixing. Although the overall accuracy of SFF dropped 20 percent, it obtained the second highest accuracy dealing with mixing pixels.

In terms of overall accuracy of the different methods, maximum likelihood classification is the best method for minerals and rocks classification using the simulated AVIRIS data (Figure 1, top left), followed by SFF and SAM; minimum distance classification and binary encoding have relative poor performance. Data sets 1 and 4 are similar to data sets 2 and 5, respectively, except that 2 and 5 have an additional uncertainty due to illumination effects. The accuracy for all methods applied to AVIRIS data, with the notable exception of minimum distance classification, declines only slightly from data sets 1 to 2 and from 4 to 5.

The results of the combined data sets are slightly more complex (Figure 1, bottom). In terms of overall accuracy, maximum likelihood classification almost achieved 100 percent accuracy for all uncertainty level data sets, and SAM resulted in the second highest accuracy. The accuracy of SFF method dropped to the third position. Minimum distance classification and binary encoding resulted in the worst accuracies. Curves of minimum distance and maximum likelihood classification follow the same trend as those from the AVIRIS data set, but the relative accuracies of the other methods differ greatly. Whereas with the simulated AVIRIS data illumination effects had little influence, with the combined data set, accuracy declined markedly when illumination was included. In fact, the illumination effects become the main factor reducing the classification accuracies. This may be a result of combining the analysis of spectra with illumination effects in the VNIR/SWIR and no illumination effects in the TIR.

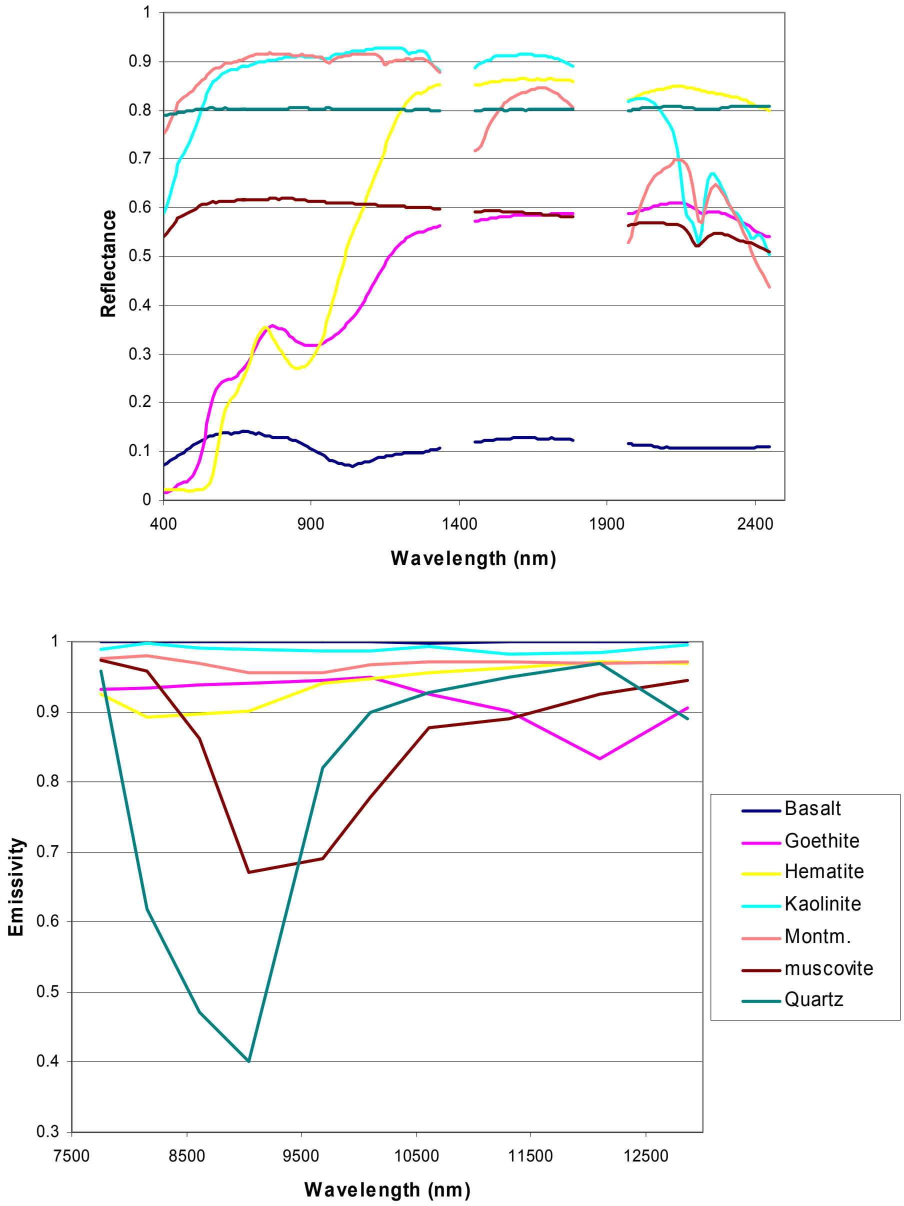

Figure 3. Laboratory reflectance spectra and emissivity spectra of minerals and rocks resampled to AVIRIS (top) and MASTER (bottom) wavelength bands. AVIRIS water absorption bands excluded from the analysis are indicated by the breaks in the spectral curves.

By comparison, maximum likelihood classification achieved the best performance on all data sets. Factors in the simulated data analysis that favor the maximum likelihood classification is the large and representative training sample of approximately 10,000 pixels, and that uncertainty in the data sets were modeled with normal distributions. In real applications, it can be difficult to select training data that completely characterize the classes of interest, and variability does not necessarily follow a normal distribution.

When the minerals and rocks with no distinct absorption features in the VNIR, SWIR, and TIR regions are excluded from the analysis, leaving just 9 minerals, the average results of the classifications (Figure 4) are similar in trend to the average results found with all 16 minerals and rocks (Figure 1), although in detail there are some important differences. Excluding the classes with relatively flat spectral curves, including basalt, raised the accuracy of most methods, especially SFF. In fact, SFF achieved the second highest position in overall accuracy applying to the simulated AVIRIS data for the 9 minerals for the moderate to high uncertainty data sets (Figure 4, upper left). Although most of the selected minerals showed absorption features in the TIR region, SFF resulted in the worst accuracy for the simulated MASTER data (Figure 4, upper right). This poor result suggests that SFF is not good for classifying multispectral data with a relative broad bandwidth, like MASTER. The results of the combined data sets (Figure 4, bottom) showed that combining AVRIS and MASTER bands made a small but notable improvement for discriminating minerals using SAM in the moderate level uncertainty data sets. Quartz, goethite, and hematite, which have distinctive absorption features in the TIR region, showed a marked increase in classification accuracy for data set 3 and 4.

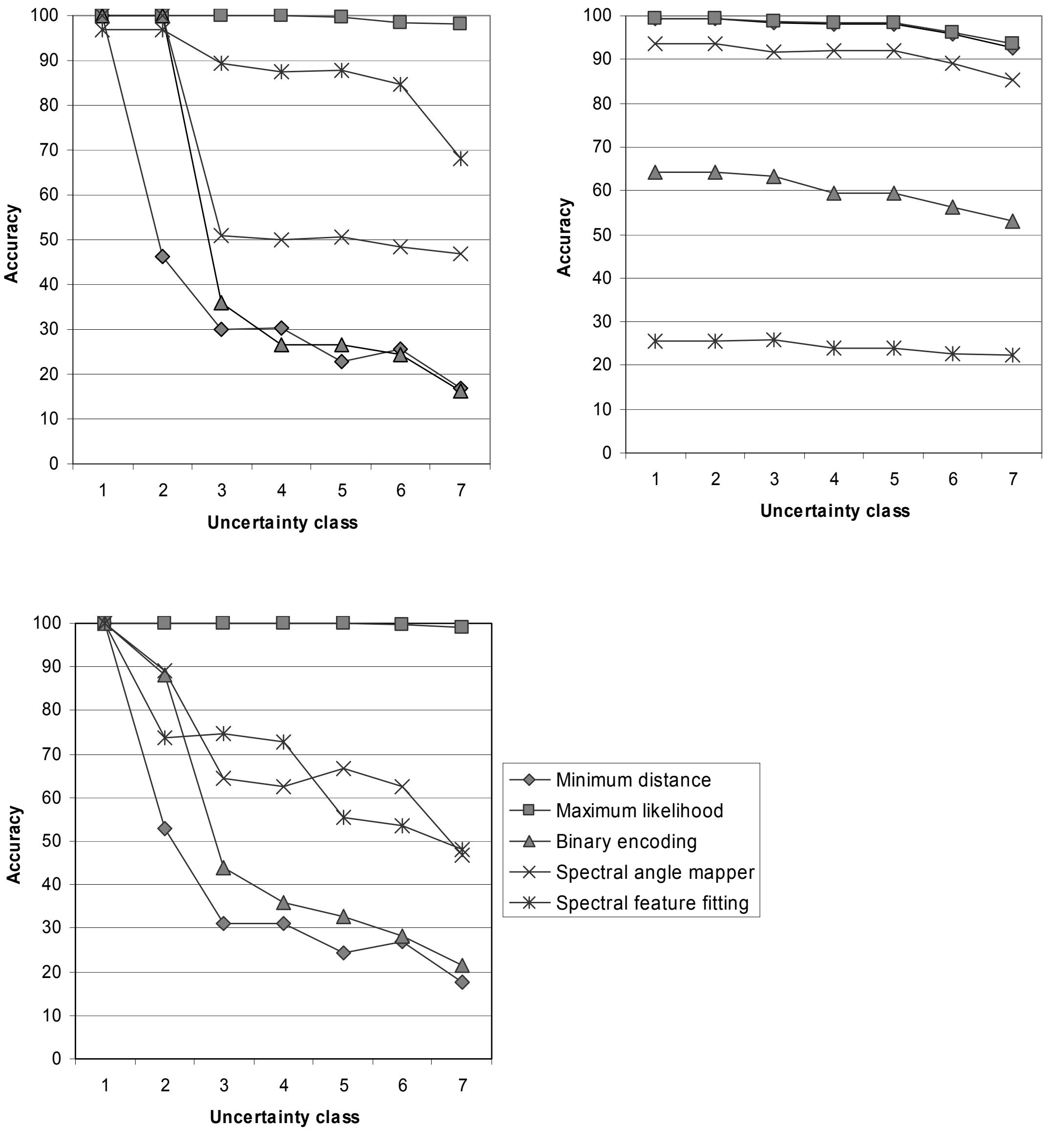

Figure 4. Comparison of the overall accuracies using five mapping methods on different noise level data sets of 9 mineral and rock classes with distinctive absorption features. Upper left: AVIRIS data sets. Upper right: MASTER data set. Bottom: Combined data set.

4. Summary and conclusions

A series of simulated data sets based on the characteristics of AVIRIS and MASTER sensors was created. The simulated data sets include surface reflectance and emissivity derived from library spectra of 16 common minerals and rocks occurring in Cuprite, Nevada. Five automatic classification algorithms, minimum distance, maximum likelihood classification, binary encoding, SAM, and SFF, were applied to all data sets. The classification results showed that combining AVIRIS with MASTER data sets can be useful for improving the accuracy of identifying the 16 selected minerals and rocks in some circumstances. First, most methods applied to the combined data sets, except SFF, achieved varying improvement in overall accuracy in comparison to these methods used with the AVIRIS data set alone. Second, some minerals and rocks showed a great improvement in their individual classification accuracies. Basalt, calcite, and muscovite, for instance, resulted in an improvement of at least 20 percent or greater in either the producer's or the user's accuracy using the combined data sets with SAM, and using the combined data set with SFF resulted in a large improvement in accuracy for goethite, hematite, quartz, and muscovite. Because SFF is an absorption feature based method, the combination of AVIRIS with MASTER with SFF only enhances discrimination of minerals and rocks exhibiting distinctive absorption features in the TIR region. Within the 16 minerals and rocks, only 4 minerals, goethite, hematite, quartz, and muscovite, have strong distinctive absorption features in TIR region. Adding uncertainty to MASTER tends to dilute absorption features. Therefore, for most minerals and rocks, combining MASTER TIR with AVIRIS bands degrades the performance of SFF.

Almost all methods used in this study are sensitive to mixing uncertainty. The only exception is maximum likelihood classification. SFF applied to the data set consisting of minerals exhibiting distinctive absorption features was found to be relative tolerant to mixing uncertainty. SAM, binary encoding, and SFF are less sensitive to illumination effects when they are applied to the simulated AVIRIS data sets. However, once illumination effects are applied to the simulated AVIRIS data in the combined data sets, there is a dramatic decrease of overall accuracy. This suggests that specific algorithms may need to be developed to integrate data with reflected and emissive characteristics, rather than simply applying previously developed methods to the combined data sets. Maximum likelihood classification is relatively robust in the presence of uncertainties, at least if sufficient training samples can be identified to estimate the probability distribution accurately. Generally however, it may not be possible to find a sufficient number of training pixels for the high dimensionality of AVIRIS data. Therefore, it may be necessary to perform feature extraction, for example with the MNF transformation, on the simulated AVIRIS and combined data sets before maximum likelihood classification is applied. The accuracy of minimum distance classification and SAM on MNF transformed data sets is almost 100 percent, indicating that the performance of MNF is very successful in suppressing the noise, and reducing the number of bands, at least for these simulated data.

In terms of overall accuracy of classification, maximum likelihood classification showed the best performance. However, prior knowledge about the study area is required in order to select training samples. Hyperspectral analysis methods like SFF have an advantage over maximum likelihood classification in that, at least potentially, external library spectra can replace in-scene training data. The simulated AVIRIS data showed that SFF is generally superior to SAM, although the accuracy of SAM applied to combined data sets is slightly better than that of SFF. SAM applied to the combined data sets increased classification accuracy for some minerals and rocks which do not exhibit distinct absorption feature in thermal infrared region, while for SFF, only the accuracy of minerals and rocks with characteristic absorption features in thermal infrared region was improved. Although binary encoding and minimum distance classification showed a relative poor performance on the simulated AVIRIS and combined data sets, binary encoding has some advantages, including a relatively simple algorithm, it is very fast, and is insensitive to illumination variation. Minimum distance classification is also relatively fast, only needs a small number of training samples, and achieves very high accuracy when it is applied to multispectral data sets. SFF is not good for multispectral data, whereas SAM can achieve relatively good performance with either hyperspectral or multispectral data.

6. Acknowledgments

The authors would like to thank Dr. S. J. Hook for advice on calculation of the signal-to-noise ratio of MASTER thermal infrared data. Three anonymous reviewers provided helpful comments and suggestions that greatly improved the quality of the manuscript. Support for this research was provided by West Virginia View.

References

Abrams, M. J., and Ashley, R. P. (1980). Alteration mapping using multispectral images—Cuprite Mining District, Esmeralda County, Nevada. *U. S. Geological Survey Open File Report,* 80–367.

Abrams, M. J., and Hook, S. J. (1991). Combined use of TIMS and AVIRIS for alteration mapping: In *Proceedings of the third Thermal Infrared Multispectral Scanner (TIMS) Workshop*, JPL Publication 91-29, Jet Propulsion Laboratory, Pasadena, California, 54–64.

Clark, R. N. (1999). Spectroscopy of rocks and minerals, and principles of spectroscopy. In A. N. Rencz (Ed.), *Remote Sensing for the Earth Sciences: Manual of Remote Sensing,* 3rd ed., Vol. 3, Chapter 1 (pp. 3–58). New York: John Wiley & Sons.

Clark, R. N., Gallagher, A. J., and Swayze, G. A. (1990). Material absorption band depth mapping of imaging spectrometer data using the complete band shape least-squares algorithm simultaneously fit to multiple spectral features from multiple materials. *Proceedings of the Third Airborne Visible/Infrared Imaging Spectrometer (AVIRIS) Workshop*, JPL Publication 90-54, Jet Propulsion Laboratory, Pasadena, California, 176–186.

Clark, R. N., Swayze, G. A., Livo, K. E., Kokaly, R. F., Sutley, S. J., Dalton, J. B., McDougal, R. R., and Gent, C. A. (2003). Imaging Spectroscopy: earth and planetary remote sensing with the USGS Tetracorder and expert systems. *Journal of Geophysical Research*, 108 (E12), 5131, doi:10.1029/2002JE001847.

Collins, J. B., and Woodcock, C. E. (1999). Geostatistical estimation of resolution dependent variance in remotely sensed images. *Photogrammetric Engineering and Remote Sensing*, 65, 41–50.

Crowley, J. K., Brickey, D. W., and Rowan, L. C. (1989). Airborne imaging spectrometer data of the Ruby Mountains, Montana: mineral discrimination using relative absorption band-depth images. *Remote Sensing of Environment*, 29, 121–134.

Ferro, C. J. and Warner, T. A. (2002). Scale and texture in digital image classification. *Photogrammetric Engineering and Remote Sensing,* 68, 51–63.

Gillespie, A.R., Rokugawa, S., Matsunaga, T., Cothern, J. S., Hook, S., and Kahle, A. B. (1998). A temperature and emissivity separation algorithm for advanced spaceborne thermal emission and reflection radiometer (ASTER) images. *IEEE Transactions on Geoscience and Remote Sensing*, 36, 1113–1126.

Goetz, A. F. H. (1989). Spectral remote sensing in geology. In: G. Asrar (ed.) *Theory and Applications of Optical Remote Sensing*, John Wiley & Sons, Inc., New York, Chapter 12. pp. 491–526.

Goetz, A. F. H., Vane, G. J., Solomon, E., and Rock, B. N. (1985). Imaging spectrometry for earth remote sensing. *Science*, 211, 1147–1153.

Green, A. A., Berman, M., Switzer, P., and Craig, M. D. (1988). A transformation for ordering multispectral data in terms of image quality with implications for noise removal. *IEEE Transactions on Geoscience and Remote Sensing*, 26, 65–74.

Green, R. O., Eastwood, M. L., Sarture, C. M., Chrien, T., Aronsson, G. M., Chippedale, B. J., Faust, J. A., Pavri, B. E., Chovit, C. J., Solis, M., Olah, M. R., and Williams, O. (1998). Imaging Spectroscopy and the Airborne Visible/Infrared Imaging Spectraometer (AVIRIS). *Remote Sensing of Environment*, 65, 227–248.

Hook, S. J., Abbott, E. Grove, A., C., Kahle, A. B., and Palluconi, F. (1999). Use of multispectral thermal infrared data in geological studies. In: A. N. Rencz (ed.), *Remote Sensing for the Earth Sciences*: *Manual of Remote Sensing*, 3rd ed., Vol. 3, Chapter 2 (pp. 59–110), New York: John Wiley & Sons.

Hook, S. J., Gabell, A. R., Green, A. A., and Kealy, P. S. (1992). A comparison of techniques for extracting emissivity information from thermal infrared data for geologic studies. *Remote Sensing of Environment*, 42, 123–135.

Hook, S. J., Karlstrom, K. E., Miller, C. F., and McCaffrey, K. J. W. (1994). Mapping the Piute Mountains, California, with thermal infrared multispectral scanner (TIMS) images. *Journal of Geophysical Research*, 99, 15,605–15,622.

Hook, S. J., Myers, J. J., Thome, K. J., Fitzgerald, M., and Kahle, A. B. (2001). The MODIS/ASTER Airborne Simulator (MASTER) – a new instrument for earth science studies. *Remote Sensing of Environment*, 76, 93–102.

Hunt, G. R. (1980). Electromagnetic radiation: the communication link in remote sensing. In B.S. Siegal and A.R. Gillespie (eds.), *Remote Sensing in Geology* (pp. 5–45). New York: Wiley.

Hunt, G. R., and Salisbury, J. W. (1974). Mid-infrared spectral behavior of igneous rocks. *Technical Report AFRCL-TR-75-0356*, US Air Force Cambridge Research Laboratory, Cambridge, Massachusetts.

Jupp, D. L., Strahler, A. H. and Woodcock, C. E. (1989). Autocorrelation and regularization in digital images. II. Simple image models. *IEEE Transactions on Geoscience and Remote Sensing*, 27, 247–258.

Kahle, A. B. (1987). Surface emittance, temperature, and thermal inertia derived from thermal infrared multispectal scanner (TIMS) data for Death Valley, California. *Geophysics*, 52, 858–874.

Kruse, F. A., Lefkoff, A. B., Boardman, J. B., Heidebrecht, K. B., Shapiro, A. T., Barloon, P. J., and Goetz, A. F. H. (1993a). The spectral image processing system (SIPS) – Interactive visualization and analysis of imaging spectrometer data. *Remote Sensing of Environment*, 44, 145–163.

Kruse, F. A., Lefkoff, A. B., and Dietz, J. B. (1993b). Expert system-based mineral mapping in Northern Death Valley, California/Nevada, Using the Airborne Visible/Infrared Imaging Spectrometer (AVIRIS). *Remote Sensing of Environment*, 44, 309–336.

Landgrebe, D. (2000). Information extraction principles and methods for multispectral and hyperspectral image data. In C. H. Chen (ed.), *Information Processing for Remote Sensing,* Chapter 1, New Jersey: World Scientific Publishing Co., Inc., River Edge.

Li, Z., Becker, F., Stoll, M. P., and Wan, Z. (1999). Evaluation of six methods for extracting relative emissivity spectra from thermal infrared images. *Remote Sensing of Environment*, 69, 197–214.

Lyon, R. J. P. (1972). Infrared spectral emittance in geologic mapping: Airborne spectrometer data from Pisgah Crater, California. *Science*, 175, 983–985.

Mueller, Richter, A., R., Habermeyer, M., Mehl, H., Dech, S., Kaufmann, H., Segl, K., Haschberger, P., and Strobl, P. (2003). ARES: a new reflective/emissive imaging spectrometer for terrestrial application: In *Proceedings of the 13th Airborne Visible/Infrared Imaging Spectrometer (AVIRIS) and Hyperion Workshop*, Jet Propulsion Laboratory, Pasadena, California.

Mustard, J. F. and Sunshine, J. M. (1999). Spectral analysis for earth science: Investigations using remote sensing data. In A. N. Rencz (ed.), *Remote Sensing for the Earth Sciences*: Manual of Remote Sensing, 3rd ed, Vol. 3, Chapter 5 (pp. 251–306), New York: John Wiley & Sons.

Pandya, M. R., Dadhwal, V. K., and Navalgund, R. R. (2000). Effects of WiFS viewing geometry on crop reflectance: A simulation study using SAIL model. *International Journal of Remote Sensing*, 21, 1931–1938.

Pouch, G. W. and Campagna, D. J. (1990). Hyperspherical direction cosine transformation for separation of spectral and illumination information in digital scanner data. *Photogrammetric Engineering and Remote Sensing*, 56, 475–479.

Price, J. C. (1979). Surface temperature variations as measured by the Heating Capacity mapping Mission. *Proceedings of the Thirteenth International Symposium on Remote Sensing of the Environ*ment (pp. 765–770). Ann Arbor, Michigan: Environmental Research Inst. of Michigan.

Richards, J.A (1993). *Remote Sensing Digital Image Analysis: An Introduction*. New York: Springer-Verlag, 340p.

Research Systems (2000). *Using IDL, IDL Version 5.6*. Research Systems, Boulder Colorado, 716p.

Research Systems (2002). *ENVI User's Guide, ENVI 3.6*. Research Systems, Boulder Colorado, 1042p.

Rowan, L. C. (1998). Analysis of simulated advanced spaceborne thermal emission and reflection (ASTER) radiometer data of the Iron Hill, Colorado, study area for mapping lithologies. *Journal of Geophysical Research D: Atmospheres*, 103, 32,291–32,306.

Salisbury, J. W., Walter, L. S., Vergo, N., and D`Aria, D. M. (1991). *Infrared (2.1–25 micrometers) Spectra of Minerals*. Johns Hopkins University Press, 294p.

Strahler, A. H., Woodcock, C. and Smith, J. A. (1986). On the nature of models in remote sensing. *Remote Sensing of Environment*, 20, 121–139.

Vane, G., Green, R. O., Chrien, T. G., Enmark, H. T., Hansen, E. G., and Porter, W. M. (1993). Airborne Visible/Infrared Imaging Spectrometer (AVIRIS). *Remote Sensing of Environment*, 44, 127–143.

Verhoef, W. (1984). Light scattering by leaf layers with application to canopy reflectance modeling: The SAIL model. *Remote Sensing of Environment*, 16, 125–141.

Vincent, R.K., and Thomson, F. J. (1971). Discrimination of basic silicate rocks by recognition maps processed from aerial infrared data. *Proceedings of the Seventh International Symposium on Remote Sensing Environment* (pp. 245–251). Ann Arbor, Michigan: University of Michigan.

Warner, T. (1999). Analysis of spatial patterns in remotely sensed data using multivariate spatial correlation. *Geocarto International,* 14: 59–65.

Warner, T. A. and Chen, X. (2001). Normalization of Landsat thermal imagery for the effects of solar heating and topography. *International Journal of Remote Sensing*, 22, 773–788.

Woodcock, C. E, Strahler, A. H., and D. L. Jupp (1988). The use of variograms in remote sensing: I. Scene models and simulated images. *Remote Sensing of Environment,* 25, 323–348.